Title

Correction of B0 and linear eddy currents: Impact on morphological and quantitative ultrashort echo time double echo steady state (UTE-DESS) imaging

Journal

NMR in Biomedicine, 36(9)

ISSN

0952-3480

Authors

Jang, Hyungseok

Athertya, Jiyo S

Jerban, Saeed

et al.

Publication Date

2023-09-01

DOI

10.1002/nbm.4939

Peer reviewed

HHS Public Access

Author manuscript

NMR Biomed. Author manuscript; available in PMC 2024 September 25.

Published in final edited form as:

NMR Biomed. ; : e4939. doi:10.1002/nbm.4939.

Correction of B_0 and Linear Eddy Currents: Impact on Morphological and Quantitative Ultrashort Echo Time Double Echo Steady State (UTE-DESS) Imaging

Hyungseok Jang, Ph.D.[1,*], **Jiyo Athertya**[1], **Saeed Jerban**[1], **Yajun Ma**[1], **Alecio F Lombardi**[1], **Christine B Chung**[1,2], **Eric Y Chang**[1,2], **Jiang Du**[1,2,3]

[1]Department of Radiology, University of California, San Diego, USA

[2]Radiology Service, Veterans Affairs San Diego Healthcare System, San Diego, USA

[3]Department of Bioengineering, University of California, San Diego, USA

Abstract

Purpose: To investigate the effects of B_0 and linear eddy currents on ultrashort echo time double echo steady state (UTE-DESS) imaging and determine whether eddy current correction (ECC) effectively resolves imaging artifacts caused by eddy currents.

Method: 3D UTE-DESS sequences based on either projection radial or spiral cones trajectories were implemented on a 3T clinical MR scanner. An off-isocentered thin-slice excitation approach was used to measure eddy currents. The measurements were repeated four times using two sets of tested gradient waveforms with opposite polarities and two different slice locations to measure B_0 and linear eddy currents simultaneously. Computer simulation was performed to investigate the eddy current effect. Finally, a phantom experiment, ex vivo experiment with human synovium and ankle samples, and in vivo experiment with human knee joints were performed to demonstrate the effects of eddy currents and ECC in UTE-DESS imaging.

Results: In a computer simulation, the two echoes (S+ and S−) in UTE-DESS imaging exhibited strong distortion at different orientations in the presence of B_0 and linear eddy currents, resulting in both image degradation as well as misalignment of pixel location between the two echoes. The same phenomenon was observed in the phantom, ex vivo, and in vivo experiments, where the presence of eddy currents degraded S+, S−, echo subtraction images, and T_2 maps. The implementation of ECC dramatically improved both the image quality and image registration between the S+ and S− echoes.

Conclusion: ECC is crucial for reliable morphological and quantitative UTE-DESS imaging.

Graphical Abstract

[*]**Corresponding Author:** Hyungseok Jang, Ph.D., University of California, San Diego, Department of Radiology, 200 West Arbor Drive, San Diego, CA 92103-8226, Phone (858) 246-2225 | Fax (858) 246-2221, h4jang@health.ucsd.edu.

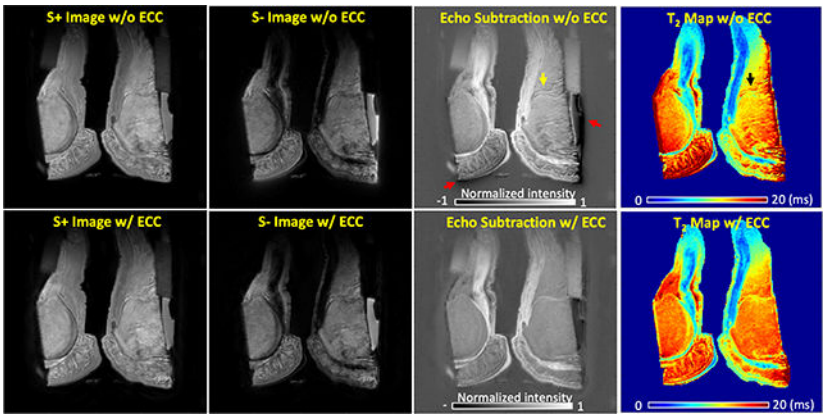

In ultrashort echo time double echo steady state (UTE-DESS) imaging, eddy current correction (ECC) dramatically improved short T_2 contrast in the weighted echo subtraction image by resolving the misalignment of pixels between the S+ and S− images (red arrows). Fine structures affected by the boundary effect were more clearly detected with ECC in the echo-subtracted image and the T_2 map (yellow and black arrows).

Keywords

eddy current; UTE; DESS; fly-back; bipolar; registration

INTRODUCTION

Double echo steady state (DESS) imaging has been investigated extensively in musculoskeletal (MSK) (1–8) and neuro (9–14) magnetic resonance imaging (MRI) because of the short scan time and flexible image contrast made possible by the combination of a free induction decay (FID)-like S+ signal and stimulated echo-based S− signal. Simple signal averaging is commonly used to combine the S+ and S− signals and has shown efficacy in delineating cartilage in MSK imaging as well as nerve in neuro imaging with high contrast. Another way to combine the S+ and S− signals is the signal model of DESS imaging based on the Bloch equation for steady state free precession, an approach which has been used to estimate both T_2 and diffusivity (15–18). More recently, ultrashort echo time (UTE)-based DESS (UTE-DESS) has been investigated in combination with either conventional 3D radial sampling or the more efficient 3D spiral cones sampling (19,20). The UTE-DESS sequence has been evaluated in morphological imaging of the human knee joint where weighted echo subtraction between S+ and S− signals achieved an image contrast that was specific to tissues with short T_2 values (so-called “short T_2 tissues”). The feasibility of T_2 mapping using UTE-DESS has also been demonstrated.

In a spin system, the residual dephasing moment of spin (or “gradient moment”) should remain unchanged by the end of each repetition time (TR) to establish steady state in transverse magnetization. In conventional DESS imaging, this can be achieved by simply rewinding the phase encoding gradients (to achieve balance) and extending the read-out gradient or applying an additional spoiling gradient in any desired direction (i.e.,

unchanged). Consequently, unipolar read-out gradients are applied to encode both S+ and S− signals. Alternatively in UTE-DESS imaging, 3D radial encoding gradients are rotated over TRs to cover a sphere of k-space. In this scheme, a pair of bipolar gradients is utilized, where the first center-out gradient (i.e., read-out) is rewinded by the second fly-back gradient (i.e., read-in). The center-out and fly-back gradients are of opposite polarity but of the same gradient moment to achieve balance. An additional spoiling gradient is interleaved to separate k-spaces for the S+ and S− signals.

In MRI, the eddy current effect is a major technical challenge that must be overcome in the pursuit of artifact-free imaging. In an electrical circuit, eddy current is generated by a time-varying magnetic field, where intensity is proportional to the slew rate and decays exponentially with a certain time constant. Given the complicated hardware structure of the modern MRI system, it is not surprising that various hardware components have the potential to generate individual eddy currents with a variety of time constants. The net eddy current of a single MRI system can be modeled as a summation of exponential decays with different time constants. The eddy current generated inversely introduces an additional magnetic field which is typically modeled as a polynomial of the spatial coordinates, namely x, y, and z (21). The 0-th order term (i.e., the constant term) is typically referred to as the B_0 eddy current, whereas the first-order term (i.e., linear to x, y, or z) is referred to as the linear eddy current. The B_0 eddy current generates a constant but time-varying magnetic field which causes additive phase error in the acquired k-space data due to a fluctuating B_0 field. The linear eddy current generates a linear magnetic field in space which mimics a gradient field, which in turn distorts a gradient waveform that results in a distorted k-space trajectory. Higher order eddy currents generate non-linearly varying magnetic fields in space, which can also cause unexpected distortion in images. Compared to conventional Cartesian imaging, UTE imaging is known to be more sensitive to eddy currents and can suffer from unwanted image artifacts such as blurriness, incorrect field of view (FOV), and morphological distortion (22,23). Previous studies have shown that eddy current correction (ECC) in UTE imaging is an effective way to avoid such issues (22–25).

For UTE-DESS imaging, Chaudhari et al. incorporated Brodski's method (26) to measure linear and B_0 eddy currents based on the Duyn's thin slice excitation scheme (27). However, to the best of our knowledge, the effect of eddy currents in UTE-DESS imaging has not yet been demonstrated in depth. Unlike conventional UTE imaging which utilizes a mono-polar readout gradient to acquire multiple gradient echoes (28), UTE-DESS utilizes a pair of balanced bipolar readout gradients (i.e., center-out and fly-back). Therefore, it is expected that S+ and S− would be affected by eddy currents with different characteristics, resulting in a discrepancy between the two echoes which could lead to critical issues in both morphological and quantitative UTE-DESS imaging. In this study, we demonstrate the effects of B_0 and linear eddy currents and further elucidate the importance of ECC for reliable UTE-DESS imaging. A thin slice excitation scheme was utilized to measure these eddy currents (26,27,29) and the effects of eddy currents and ECC were demonstrated in a phantom experiment, ex vivo experiment with human synovium and ankle specimens, and in vivo experiment with human knee joints.

METHODS

Pulse sequence - UTE-DESS

Figures 1A and 1B illustrate pulse sequences for UTE-DESS imaging. Our UTE-DESS sequence was implemented on a 3T clinical MR system (MR750, GE Healthcare, Milwaukee, WI, USA) which can be operated in two different modes: 3D projection radial (PR) mode (Figure 1A) and 3D spiral cones mode (Figure 1B). “PR-mode” can be achieved by straightening the spiral arms. Note that the encoding gradients are designed differently for each cone (with a unique polar angle) which allows more efficient encoding for anisotropic imaging. In our implementation of the UTE-DESS sequence, 16 sets of gradients for 16 basis cones were initially generated. The gradient waveforms in other polar angles (typically ~100–200 cones) were generated by linearly combining the 16 basis gradient sets. We implemented this approach to prevent potential memory issues on the scanner and to speed up the pulse generation, thereby reducing scan preparation time.

To achieve steady state magnetization in UTE-DESS, a short hard radiofrequency (RF) pulse is repetitively applied at every TR (Figures 1A and 1B). Balanced bipolar read-out/read-in gradients, interleaved by a spoiling gradient, are applied. The read-out/read-in gradients rotate over TRs to cover each conical surface, while the spoiling gradients remain unchanged. In contrast with conventional UTE imaging where the minimum echo time (TE) is determined by RF coil deadtime (i.e., blind time following a RF pulse due to the RF mode switching between transmit and receive), the minimum TE in UTE-DESS imaging is determined by additional delay factors in the MR system including gradient delay, RF deadtime before and after RF pulse, and preparation time before the next TR. In the MR system used in this study (GE MR750), the minimum TE was 84 μs. Though the maximum gradient amplitude allowed by this clinical whole-body scanner was 50 mT/m, this parameter was further constrained to 90% of the hardware maximum (i.e., 45 mT/m) for the UTE-DESS sequence to ensure safe operation as well as linearity of the gradient field.

ECC based on thin slice off-isocenter excitation

Figures 1C and 1D show the pulse sequences that were used to measure the B_0 and linear eddy currents at the same time for UTE-DESS in PR-mode and cones-mode, respectively. The ECC is based on measurement of the phase evolution within a thin slice excited at an off-isocentered location (26,27,29). While the example portrayed in Figures 1C and 1D show two bipolar encoding gradients being used specifically in PR-mode or cones-mode, these encoding gradients can be replaced with any gradient waveform. Unfortunately, it is very difficult to precisely model the eddy currents generated from all the signal pathways in DESS imaging because the steady state S+ and S− signals are produced by FID and stimulated echoes that originate from multiple pathways. Therefore, our study targeted investigation of short-lasting eddy currents, and ECC was performed based on two bipolar read-out/read-in gradients. ECC for the spoiling gradient was not considered under the assumption that the effects of eddy currents from the spoiling gradient are balanced and, therefore, canceled on the pathway towards forming the S− signal (i.e., time-reversed). This is a reasonable proposition given that the spoiling gradient remains unchanged throughout the imaging process.

To simultaneously measure B_0 and linear eddy currents, the measurements were repeated with four different settings as proposed by Brodsky et al. (26): two opposite gradient polarities, G and −G (orange and blue lines, respectively, in Figures 1C and 1D), and two different locations of slice selection, x_0 and $-x_0$ (green and red lines, respectively, in Figures 1C and 1D). Based on these four measurements, k-space trajectory, $\hat{k}$, and the phase error induced by the B_0 eddy currents, $\hat{\phi}$, under the prescribed gradient waveform, are calculated based on the simple algebraic equations,

$$\hat{k}(t) = (\psi(G, x_0, t) - \psi(-G, x_0, t) - \psi(G, -x_0, t) + \psi(-G, -x_0, t))/(4x_0)$$

and

$$\hat{\phi}(t) = (\psi(G, x_0, t) - \psi(-G, x_0, t) + \psi(G, -x_0, t) - \psi(-G, -x_0, t))/4, \quad (1)$$

where $\psi(G, x_0, t)$ is phase information at an encoding time delay, t, measured with a gradient waveform, G, and a slice location, x_0.

Because it is prohibitively time-consuming to measure all spokes for 3D imaging (which typically number between ~5,000 and 80,000 spokes), our study used a more time-efficient approach based on the linear time invariant (LTI) assumption of a gradient system. With this approach, only basis gradient waveforms need to be measured, though it's notable that the rotation of each spoke must be considered to compensate for not only rotation in the x-y plane (which is intended to cover a conical surface in 3D cones imaging) but also rotation that is due to the oblique logical imaging plane. Therefore, gradient waveform measurements must be repeated in all three physical axes to capture any changes to $\hat{k}$ and $\hat{\phi}$ that may be induced by rotation.

$\hat{G}_{i,j,x}$, $\hat{G}_{i,j,y}$, and $\hat{G}_{i,j,z}$ are defined as the *i*-th gradient waveform (with $i = 1$, 2, and 3 corresponding to the generated x, y, and z gradient waveforms) in the *j*-th cone (with $j = 1$ through 16 in this study), measured in the physical x, y, or z axis. For example, $\hat{G}_{3,2,x}$, indicates the z-gradient (i.e., $i = 3$, which corresponds to the z gradient waveform) in the second basis cone measured in the physical x-axis. The same convention is used for $\hat{k}$ and $\hat{\phi}$. The rotated gradient waveform can be expressed as a linear combination of the measured gradients as follows:

$$\hat{G}_{x,j}(\varphi) = r_{11}\left(\hat{G}_{1,j,x}cos\varphi + \hat{G}_{2,j,x}sin\varphi\right) + r_{12}\left(-\hat{G}_{1,j,x}sin\varphi + \hat{G}_{2,j,x}cos\varphi\right) + r_{13}\hat{G}_{3,j,x},$$

$$\hat{G}_{y,j}(\varphi) = r_{21}\left(\hat{G}_{1,j,y}cos\varphi + \hat{G}_{2,j,y}sin\varphi\right) + r_{22}\left(-\hat{G}_{1,j,y}sin\varphi + \hat{G}_{2,j,y}cos\varphi\right) + r_{23}\hat{G}_{3,j,y},$$

and

$$\hat{G}_{z,j}(\varphi) = r_{31}\left(\hat{G}_{1,j,z}cos\varphi + \hat{G}_{2,j,z}sin\varphi\right) + r_{32}\left(-\hat{G}_{1,j,z}sin\varphi + \hat{G}_{2,j,z}cos\varphi\right) + r_{33}\hat{G}_{3,j,z}, \quad (2)$$

where φ is the in-plane angle to rotate a radial or spiral spoke in the logical x-y plane. r_{mn} represents an element in the m-th row and n-th column in a 3×3 rotation matrix, R, which transforms a coordinate from the logical imaging plane to the physical gradient plane. $\widehat{G}_{x,j}(\varphi)$, $\widehat{G}_{y,j}(\varphi)$, and $\widehat{G}_{z,j}(\varphi)$ denote the rotated gradient waveforms for the j-th basis cone within the noted physical coordinate system after in-plane rotation with an angle of φ.

In this study, $\widehat{k}$ and $\widehat{\phi}$, not gradients, were directly measured. However, the same linear combination as in Equation 2 can be directly applied to calculate $\widehat{k}$ and $\widehat{\phi}$ with any rotations because $\widehat{k}$ is determined by integration of the gradient, and $\widehat{\phi}$ is determined by the first derivative of the gradient in the time domain. Detailed equations can be found in the Appendix.

Computer simulation

To demonstrate the issue caused by eddy currents in bipolar radial gradient recalled echo (GRE) acquisition, a 2D computer simulation was performed using Matlab R2017b (MathWorks, Natick, MA, USA). First, a 2D digital phantom (i.e., Shepp-Logan phantom) was generated for input. Then, trapezoidal gradients were generated for 2D radial imaging using the following parameters: FOV = 240 × 240 mm^2, matrix = 256 × 256, 401 spokes, maximum gradient slew rate = 150 mT/m/ms, maximum gradient amplitude = 30 mT/m, readout bandwidth (rBW) = 250 kHz, dwell time = 4 μs, and the number of sampling points in a spoke = 246 with 2x oversampling. Based on the simulated gradients and the corresponding k-space trajectories, the reference phantom image was resampled using non-uniform fast Fourier transform (NuFFT) to produce the reference k-space data.

To simulate linear eddy current, a simple impulse response based on single exponential model, $h_e(t)$ was adopted as follows:

$$h_e(t) = \begin{cases} me^{-t/\tau_c} & t \geq 0 \\ 0 & t < 0 \end{cases}, \quad (3)$$

where m denotes magnitude of the eddy current and τ_c denotes time constant of the exponential decay in the impulse response. The parameters for this simulated eddy current were based on measurements reported in the literature (29–31): the B_0 eddy current was simulated with τ_c of 300 μs and m of 0.5×10^{-3} (29,30), while the linear eddy current was simulated with τ_c of 100 μs and m of 5×10^{-3} (30,31). Though, in reality, impulse response typically results from a combination of eddy currents with different time constants and amplitudes, this experiment simulated only a single component for the purposes of demonstration.

The simulated impulse response was then convolved with the first derivative of the input gradient to yield the B_0 and linear eddy currents as follows:

$$B_e(t) = -\frac{dG(t)}{dt} \otimes h_e(t), \quad (4)$$

where $G(t)$ is an input gradient and $\otimes$ is a convolution operator. The magnetic field, $B_e(t)$, generated by the linear eddy current is equivalent to the additional (gradient field-distorting) gradient shape, $G(t)$. Therefore, the distorted gradient was calculated as $G(t) + B_e(t)$. Using the resultant distorted k-space trajectory, the 2D digital phantom image was resampled to yield k-space data using an inverse gridding scheme. The B_0 eddy current causes accumulated phase error over encoding time, t_e, which can be modelled as $\gamma \int_0^{t_e} B_e(t)dt$ (where γ = the gyromagnetic ratio of a proton). The phase error calculated at each t_e was then added to the corresponding k-space data to simulate the B_0 eddy current's effect.

Imaging Experiments

The UTE-DESS sequence was implemented on a 3T clinical MR system (GE MR750) to evaluate the effects of eddy currents and the efficacy of ECC in phantom, ex vivo, and in vivo experiments. In the phantom experiment, a GE resolution phantom was used. In the ex vivo experiments, human synovium tissue from a total knee replacement surgery (60-year-old patient with osteoarthritis) and three cadaveric human ankle specimens (39-, 41-, and 91-year-old donors) were scanned. In the in vivo experiment, the knee joints of five healthy volunteers (aged 40.6 ± 7.1) were scanned. All human subjects research was performed in compliance with the guidelines of the Human Research Protections Program at the University of California, San Diego, and written informed consent forms were collected from all subjects.

The GE phantom was scanned using a body coil with the following imaging parameters for UTE-DESS imaging: 1) 3D PR trajectory: flip angle (FA) = 20 °, FOV = 200 × 200 × 120 mm^3, matrix = 200 × 200 × 60, rBW = 250 kHz, TR = 5 ms, nominal TE for S+ (TE_{S+}) = 88 μs, number of spokes = 64,807, and scan time = 5 minutes 24 seconds, 2) 3D spiral cones trajectory: parameters matched to PR-mode except for number of spokes = 23,009 and scan time = 1 minutes 55 seconds.

For the ex vivo synovium experiment, the harvested synovium tissue was soaked in saline in a 30-mL syringe, then scanned using a homemade 30cc transmit/receive solenoid coil with the following imaging parameters for UTE-DESS imaging with 3D spiral cones trajectory: FA = 30 °, FOV = 60 × 60 × 32 mm^3, matrix = 200 × 200 × 80, rBW = 125 kHz, TR = 21 ms, TE_{S+} = 88 μs, number of spokes = 90,911, and scan time = 31 minutes 41 seconds.

For the ex vivo ankle experiment, the posterior sides of three fresh-frozen ankle specimens were dissected to include the entire Achilles tendon and most of the calcaneus bone. The specimens were cut while frozen using a commercial bandsaw, then soaked in fomblin to minimize dehydration and air-tissue susceptibility. MRI was performed using a transmit/receive birdcage wrist coil (Mayo Clinic, Rochester, MN, USA) with the following parameters for UTE-DESS with 3D spiral cones trajectory: FA = 10 °, FOV = 120 × 120 × 100 mm^3, matrix = 220 × 220 × 50, rBW = 125 kHz, TR = 8.1 ms, TE_{S+} = 88 μs, number of spokes = 60,277, and scan time = 8 minutes 9 seconds.

For the in vivo knee experiment, five healthy volunteers underwent knee imaging with an 8-channel transmit/receive knee coil (GE Healthcare) with the following imaging parameters

for UTE-DESS with 3D spiral cones trajectory: FA = 10 °, FOV = 130 × 130 × 120 mm^3, matrix = 256 × 256 × 60, rBW = 250 kHz, TR = 4.9 ms, TE_{S+} = 88 μs, number of spokes = 58,303, and scan time = 4 minutes 46 seconds.

The eddy currents were measured for each acquisition using a body coil with the following imaging parameters: slice location (x_0) = 20 mm, slice thickness = 0.3 mm, FA = 20 °, TR = 50 ms, number of excitations (NEX) = 10, and scan time = 4 minutes 48 seconds. The eddy current measurement was performed only once when the protocol was initially set up.

Data Processing

The data acquired for ECC were processed using Matlab. First, the raw phase data was processed with a 1D phase unwrapping algorithm provided in Matlab, then a simple algebraic calculation proposed by Brodsky et al. (26) was performed to yield k-space trajectory, $\hat{k}$, and the phase error induced by the B_0 eddy currents, $\hat{\phi}$, for all basis gradients. Then, the measured $\hat{k}$s and $\hat{\phi}$s were linearly combined based on Equations A1–A4 to yield k-space trajectories and phase errors for all spokes.

All UTE-DESS images were reconstructed offline using homemade codes written in Matlab based on NuFFT (32). The images were reconstructed with nominal k-space trajectory and measured k-space trajectory, respectively, to evaluate the efficacy of ECC for the linear eddy currents, and with or without correction of $\hat{\phi}$.

To demonstrate the effect of ECC in parameter mapping, a simple T_2 mapping based on a spin echo model was performed using the S+ and S− images based on the equation $T_2 = -(2TR - 2TE_{S+})/\ln(S-/S+)$, without corrections for B_1 inhomogeneity or diffusion weighting. Between T_2 maps without ECC (T_2) and with ECC ($T_{2,\,ECC}$), absolute error was calculated as $|T_2 - T_{2,\,ECC}|$, and percent error was calculated as $|T_2 - T_{2,\,ECC}|/T_{2,\,ECC}$ x100. In three ex vivo ankle joints and five in vivo knee joints, regions of interest (ROIs) were manually drawn in the Achilles tendon and patellar tendon, respectively, based on the images acquired with ECC. The mean values of the T2 parameters without and with ECC were calculated.

RESULTS

Computer Simulation

Figure 2A shows a simulated linear eddy current with a given trapezoidal readout gradient used for the simulation of S+. The linear eddy current in the S− echo, not shown in the figure, was simulated by using the same gradient waveform in the opposite polarity and yielded an eddy current in the opposite direction. Figures 2B and 2C show the simulated k-space trajectory for S+ and S−, respectively, on a normalized scale (i.e., 1.0 corresponds to the k-space coordinate for a desired spatial resolution that is 500 cycles/meter in this simulation). The k-space trajectory deviated from the nominal trajectory due to the linear eddy current. The trajectory for S− (Figure 2C) showed a higher degree of distortion due to the error accumulated during a longer signal pathway: center-out followed by fly-back. Figures 2D, 2E, and 2F show simulated phase error, $\hat{\phi}$, maps induced by B_0 eddy current in the S+ and S− acquisitions, and 1D profiles of the resultant point spread functions (PSFs).

For the S+ acquisition, a nearly linear phase error was exhibited in the diagonal direction of k-space (Figure 2D), while a more complicated non-linear phase error was exhibited in the S− acquisition (Figure 2E). This is because B_0 eddy current accumulates in a longer signal pathway for S− echo. A central 1D profile of the resultant PSFs (Figure 2F) shows a discrepancy where the PSFs are shifted in opposite directions between S+ and S−, a consequence of the phase error ramping in opposite diagonal directions in S+ and S−, as shown in Figures 2D and 2E.

The reconstructed images from the computer simulation are shown in Figure 3A. The S+ image was less affected by the linear and B_0 eddy currents than the S− image. Figure 3B shows a strong boundary effect in the diagonal direction in the difference image between S+ and S−, implying misalignment of pixels due to the shift in opposite directions. This confirms the findings of Figure 2.

Phantom Experiment

Figure 4 shows results from the phantom experiment based on PR-mode UTE-DESS imaging. Figure 4A shows the measured trajectory for an exemplary radial spoke on a k-space plane at $k_z = 0$. A slightly derated trajectory was observed, but no dramatic deviation was shown in either the S+ or S− trajectory. The measured $\widehat{\phi}$ showed nearly linear and non-linear phase error across k-space for S+ and S−, respectively (Figure 4B). The phase error in Figure 4B spanned from approximately −0.7 to 0.7 radians, similar to the patterns estimated during the previously performed computer simulation (Figures 2D and 2E). The difference image without ECC in Figure 4C shows strong boundary effect due to misalignment of pixels in the diagonal direction caused by the B_0 eddy current effect, an issue that was dramatically reduced when ECC was used to remove the phase error across k-space.

Similar results were obtained with cones-mode UTE-DESS imaging. Figure 5 shows results from the same phantom imaged using cones-mode. As in PR-mode, the measured k-space trajectory was slightly derated compared to the nominal trajectory (Figure 5A), but the pattern and direction of phase error, $\widehat{\phi}$, were different from those resulting from PR-mode (Figure 5B). While PR-mode yielded phase ramping in exactly opposite directions (i.e., a 180° difference), spiral cones-mode yielded a phase error that was not quite entirely in the opposite direction (i.e., ~90° in S+ and ~225° in S−). The reconstructed images with measured trajectory showed a slightly smaller FOV due to the derated k-space trajectory (Figure 5C), a phenomenon that was also observed in the computer simulation (Figure 3A) and PR-mode imaging (Figure 4C). Overall, there was no dramatic improvement in image quality observed with linear eddy current correction alone (i.e., with measured k-space trajectory). In the S− image, a blurriness artifact was visible in the boundary of the phantom (white arrows in Figure 5C), which was clearly removed with $\widehat{\phi}$ correction. As was the case in PR-mode, a boundary effect was also exhibited (black arrows in Figure 5C), though dramatically reduced when ECC was applied to improve pixelwise registration between the S+ and S− echoes.

Supporting Figure S1 shows the measured k-space trajectory and $\widehat{\phi}$ in the cones-mode UTE-DESS, which was obtained at two different time points 54 days apart. Little deviation

was observed between the two measurements, and the high stability of the measurement is consistent with reports from Vannesjo et al. (33).

Ex Vivo Human Synovium Tissue Experiment

Figure 6 shows images of synovium tissue from the human knee joint acquired with UTE-DESS in 3D cones-mode. The overall image quality was dramatically improved by ECC, especially for the S− image. Overall, the measured trajectory did not yield any noticeable improvement, though $\widehat{\phi}$ correction suppressed the blurriness artifact near the boundary of the syringe (green arrow). The S− image with $\widehat{\phi}$ correction is also clearer, and there is a noticeable reduction in low frequency signal bias across both the syringe and synovium tissue. Some errors remained even after ECC, presumably due to the nonlinearity of the gradient system, as well as imperfection or noise in the ECC measurement (a red arrow).

Ex Vivo Human Ankle Sample Experiment

Figure 7 shows UTE-DESS images of human ankle specimens. ECC dramatically improved short T_2 contrast in the weighted echo subtraction image by resolving the misalignment of pixels between the S+ and S− images (red arrows). Fine structures affected by the boundary effect were more clearly detected with ECC in the echo-subtracted image and the T_2 map (yellow and black arrows). The absolute error and percent error in T_2 mapping induced by eddy currents are demonstrated in Figures 7I and 7J, which show strong error near tissue boundaries (white arrows). For all specimens, the estimated T2 parameters in the Achilles tendon were 6.4 ± 0.7 ms without ECC and 5.6 ± 0.9 ms with ECC.

In Vivo Human Knee Joint Experiment

ECC dramatically improved depiction of short T_2 tissues in the echo subtraction images of study participants, greatly reducing boundary artifact and signal bias. Figure 8 shows the results from a representative healthy volunteer. ECC improved short T_2 contrast in the echo subtraction image with dramatically suppressed boundary effects, resulting in improved depiction of the patellar tendon, quadriceps tendon, osteochondral junction, anterior cruciate ligament, and posterior cruciate ligament (red and green arrows in Figures 8C and 8G). However, there was a residual boundary effect observed in the images with ECC, presumably due to ECC imperfections related to the nonlinearity of the gradient system or a concomitant gradient field (yellow arrows in Figure 8G). The T_2 map without ECC showed strong boundary artifacts near tissue interfaces where unreliable T_2 values were estimated (e.g., negative values—which are not physically meaningful—were estimated near the patellar tendon, indicated by a white arrow in Figure 8D). ECC dramatically reduced this effect (Figure 8H). Figures 8I and 8J show the resultant error maps in T_2, which exhibit strong error near the tissue boundaries as a result of the eddy currents (white arrows). For all volunteers, the estimated T2 parameters in the patellar tendon were 14.0 ± 0.8 ms without ECC and 10.4 ± 0.7 ms with ECC.

DISCUSSION

In this study, we showed the importance of ECC in UTE-DESS imaging. In a computer simulation, the presence of eddy currents resulted in pixel misalignment which led to strong

morphological differences between the S+ and S− images (Figure 3B). This effect is mainly due to phase modulation in the acquired k-space data caused by B_0 eddy currents shifting the B_0 field, a phenomenon explained by the Fourier shift theorem: linear phase modulation in the k-space domain is equivalent to pixel shift in the spatial domain, and vice versa. In UTE-DESS, different phase modulations in the acquired k-space data may result in different shift effects between the S+ and S− echoes, causing misregistration of pixels. Moreover, non-linear phase modulation in S− echo may cause image degradation.

In the phantom, ex vivo, and in vivo experiments, artifactual misregistration was observed between the S+ and S− echoes. Moreover, B_0 eddy currents degraded the overall image quality of the S− echo, with representative blurriness and signal bias artifacts shown in Figures 5C, 6C, and Figure 7B. Those artifacts were significantly reduced by the incorporation of ECC. B_0 eddy currents were the primary factor affecting image quality and image registration between the two echoes, so correcting only the linear eddy currents neither improved image quality nor resolved the pixel misalignment issue (Figures 4, 5, and 6). A large portion of the linear eddy currents in our imaging experiments were compensated for by the vendor's own MR system pre-emphasis gradient tuning and delay correction (adjustment of the data acquisition timing to yield optimal image quality) which were set up upon installation of our UTE-DESS sequence.

In this study, we demonstrated whole organ pixelwise T_2 mapping with UTE-DESS for the first time, which requires accurate ECC across the whole imaging region. The efficacy of ECC for quantitative UTE-DESS imaging was demonstrated with a simple T_2 mapping as shown in Figures 7 and 8. The spatial variation and boundary effect in the parameter maps were much reduced with ECC (Figures 7G and 7H). Without ECC, the pixelwise parameters near the tissue boundary were misestimated (showing negative values) due to the misregistration of S+ and S− images which caused an abrupt signal change between the two echoes (Figure 8D). In the ex vivo experiment with human ankle specimens, the error in the measurement of T_2 parameter in the Achilles tendons caused by eddy currents was over 10% (5.6 ms without ECC vs. 6.4 ms with ECC) which was also well demonstrated in Figures 7I and 7J. In the in vivo experiment, the error of T2 estimation caused by ECC was over 30% in the patellar tendon (14.0 ms without ECC vs. 10.4 ms with ECC). Note that the T_2 mapping in this study was performed with a simple signal model based on spin-echo, which did not consider the effect of additional diffusion-weighting or the contribution of stimulated echoes. Therefore, the estimated T_2 parameter maps may have been affected by additional errors. More accurate parameter estimation of T_1, T_2, and diffusivity with quantitative UTE-DESS based on the SSFP signal model (34) and extended phase graph approach (15) remains to be investigated.

In UTE-DESS imaging, echo subtraction can be performed between the S+ and S− images to suppress long T_2 tissues and thereby accentuate short T_2 tissues or tissues with high diffusivity (19,35). However, the final image quality can be critically affected if the pixel misalignment effect caused by the eddy currents is left unaddressed. This issue can also be problematic when performing quantitative parameter mapping (34,36), where adequate image registration is a prerequisite. ECC is, therefore, an essential step for the integrity of these scans. Similar B_0 eddy current-induced issues were recently reported by Robison

et al. (29). In their study, 2D spiral imaging was performed utilizing spiral-in and spiral-out acquisition at the same time. Due to the different phase modulations in the k-space data acquired with spiral-in and spiral-out trajectories, the image reconstructed from the combined k-space data without B_0 eddy current correction showed blurriness near the tissue boundaries. Note that this can also be considered a general issue for either standard UTE imaging that utilizes a pair of center-out and fly-back gradients (37) or Cartesian imaging that utilizes bipolar readout gradients (38).

Unfortunately, the conventional method for direct measurement of eddy currents is extremely time-intensive and therefore not feasible for 3D UTE imaging where approximately 5,000 to 80,000 spokes may be acquired. Therefore, we applied the LTI assumption and measured a reduced set of basis gradients (i.e., 16 sets of gradients) such that only repeat measurement of three gradient waveforms in the physical axes (i.e., gradients applied to the x, y, and z axes) was required. While this required a scan time that was three times longer per spoke, only 16 spokes were measured, so the overall scan time for ECC was much more feasible (<5 minutes) compared to what is required when measuring the typical 5,000 to 80,000 spokes. Note that the overall measurement only needs to be performed once when a new protocol is set up, such that it does not interfere with the UTE-DESS imaging workflow (i.e., no extra scan time is needed). This approach also affords flexibility regarding the rotation of the logical imaging plane, something that is not feasible in the direct measurement approach.

Although the simple LTI system-based method provides some degree of reproducibility, the measurement for ECC should be done if different gradient waveforms are used for imaging (e.g., when using different FOV, matrix size, and rBW). A gradient impulse response function (GIRF)-based approach (23,29,33,39) can be an alternative for a more reproducible ECC. Multiple gradient blips with different durations (23,29,33) or frequency sweeping Chirp gradients (39) can be used to measure GIRF, but this requires additional expertise in pulse sequence programming and signal processing. Moreover, external hardware is often necessary (or at least optimal) for ensuring reliable measurement of GIRF (21). One limitation of an LTI-based method is that there is no ability to compensate for errors caused by the nonlinearity of the gradient system, which results in the imperfect ECC demonstrated in Figures 6 and 8. The nonlinearity of the gradient system typically includes inherent spatial or temporal distortion because the gradient system is designed to guarantee a good linear magnetic field that is close to the isocenter. The gradient system also induces undesired non-linear spatially varying magnetic fields (concomitant gradients) (40,41). In our future studies, we will investigate ECC for UTE-DESS imaging further in this regard, including the effects of GIRF and higher order eddy currents.

In this study, we only considered short-term eddy currents from encoding gradients. A spoiling gradient between the two encoding gradients was not considered, under the assumption that the dephasing caused by the spoiling gradient is canceled (i.e., rephased) in the refocusing pathway (time-reversed) because the gradient waveform remains the same, therefore creating the same eddy current effect. Furthermore, it still remains to be seen how long-term eddy currents affect steady state, given that it is achieved by signals from multiple preceding pathways. To understand this, it would be necessary to perform eddy current

measurement in DESS mode; however, because a long sinc pulse is used to excite a thin slice in Brodsky's method based on Duyn's method (27), UTE imaging is prevented by the long isodelay (typically a half of the pulse width). One alternative may be the single point imaging (SPI)-based method (23) which can be achieved by simply scaling the encoding gradients without modification of the RF pulse, a change that does not spoil the steady state. However, a previous study by Jang et al. demonstrated this but only presented linear ECC. Further investigation would be necessary to achieve B_0 ECC using the SPI-based method. A more feasible option may be to use field monitoring equipment for direct measurement of GIRF that could be used to perform indirect measurement of long-term eddy currents. In future studies, we will investigate ECC for UTE-DESS imaging further in this regard.

Finally, it is worth noting that UTE-DESS is the promising technique capable of T_2 mapping of short-T_2 tissues using a clinical whole-body scanner. Short-T_2 tissues such as the Achilles tendon are "invisible" with conventional clinical MRI sequences and their T_2 values are unknown (42). The regular UTE sequences can only provide T_2* mapping, which is more sensitive to the field inhomogeneity and susceptibility effects and likely less robust than T_2 mapping. UTE-DESS has many potential applications. For example, osteoarthritis (OA) is a whole-organ disease involving damage to not only the articular cartilage, but also to the menisci, ligaments, tendons, subchondral bone-cartilage interface, and subchondral bone (43). The failure of any of those tissues may affect others and thereby contributes to failure of the joint as a whole. However, the menisci, ligaments, tendons, and bone all have short T_2 values, and are largely "invisible" with clinical MRI sequences (42). Their contribution to OA is underestimated. UTE-DESS with ECC makes the "invisible" tissues "visible" and provides robust T_2 mapping for all major joint tissues, thereby greatly improving the diagnosis and therapeutic monitoring of OA and many other joint diseases.

CONCLUSION

In this study, we investigated the effects of the B_0 and linear eddy currents, as well as the efficacy of ECC for UTE-DESS imaging. ECC significantly improved image quality and the image registration between S+ and S− echoes, which are both crucial for more reliable morphological and quantitative UTE-DESS imaging.

Supplementary Material

Refer to Web version on PubMed Central for supplementary material.

ACKNOWLEDGEMENTS

The authors acknowledge grant support from the NIH (R01 AR075825, R01AR062581, R01AR068987, R01AR078877, R01AR079484, R21AR075851, P30AR073761, and K01AR080257), Veterans Affairs Clinical Science Research and Development (Merit Awards I01CX002211, I01CX001388, I01RX002604, and I01CX000625), and GE Healthcare.

DATA AVAILABILITY STATEMENT

The data that support the findings of this study are available from the corresponding author upon reasonable request.

APPENDIX

The measured k-space trajectory in a physical plane can be calculated by:

$$\hat{k}_{x,j}(\varphi) = r_{11}\left(\hat{k}_{1,j,x}cos\varphi + \hat{k}_{2,j,x}sin\varphi\right) + r_{12}\left(-\hat{k}_{1,j,x}sin\varphi + \hat{k}_{2,j,x}cos\varphi\right) + r_{13}\hat{k}_{3,j,x}\,,$$

$$\hat{k}_{y,j}(\varphi) = r_{21}\left(\hat{k}_{1,j,y}cos\varphi + \hat{k}_{2,j,y}sin\varphi\right) + r_{22}\left(-\hat{k}_{1,j,y}sin\varphi + \hat{k}_{2,j,y}cos\varphi\right) + r_{23}\hat{k}_{3,j,y}\,,$$

and

$$\hat{k}_{z,j}(\varphi) = r_{31}(\hat{k}_{1,j,z}cos\varphi + \hat{k}_{2,j,z}sin\varphi) + r_{32}(-\hat{k}_{1,j,z}sin\varphi + \hat{k}_{2,j,z}cos\varphi) + r_{33}\hat{k}_{3,j,z}\,, \tag{A.1}$$

where $\hat{k}_{x,j}(\varphi)$, $\hat{k}_{y,j}(\varphi)$, and $\hat{k}_{z,j}(\varphi)$ denote the measured k-space trajectory after the in-plane rotation with an angle of φ for *j*-th cone in a physical plane. To use this for image reconstruction, the k-space trajectories should be converted back to the logical plane, which can be done by applying a rotation matrix, R:

$$\widehat{K}_j(\varphi) = R^T\left[\hat{k}_{x,j}(\varphi)\ \hat{k}_{y,j}(\varphi)\ \hat{k}_{z,j}(\varphi)\right]^T, \tag{A.2}$$

Where $\widehat{K}_j(\varphi)$ is a vector containing a 3D k-space trajectory with a rotation angle, φ, in *j*-th cone. $\hat{\phi}$ can be calculated using the same approach as follows:

$$\hat{\phi}_{x,j}(\varphi) = r_{11}\left(\hat{\phi}_{1,j,x}cos\varphi + \hat{\phi}_{2,j,x}sin\varphi\right) + r_{12}\left(-\hat{\phi}_{1,j,x}sin\varphi + \phi_{2,j,x}cos\varphi\right) + r_{13}\phi_{3,j,x}\,,$$

$$\hat{\phi}_{y,j}(\varphi) = r_{21}\left(\hat{\phi}_{1,j,y}cos\varphi + \hat{\phi}_{2,j,y}sin\varphi\right) + r_{22}\left(-\hat{\phi}_{1,j,y}sin\varphi + \hat{\phi}_{2,j,y}cos\varphi\right) + r_{23}\hat{\phi}_{3,j,y}\,,$$

and

$$\hat{\phi}_{z,j}(\varphi) = r_{31}(\hat{\phi}_{1,j,z}cos\varphi + \hat{\phi}_{2,j,z}sin\varphi) + r_{32}(-\hat{\phi}_{1,j,z}sin\varphi + \hat{\phi}_{2,j,z}cos\varphi) + r_{33}\hat{\phi}_{3,j,z}\,, \tag{A.3}$$

where $\hat{\phi}_{x,j}(\varphi)$, $\hat{\phi}_{y,j}(\varphi)$, and $\hat{\phi}_{z,j}(\varphi)$ denote the measured phase error due to the B_0 eddy currents for a gradient rotated with an angle of φ in *j*-th cone. The total phase error, $\hat{\phi}_j(\varphi)$, caused by a gradient with in-plane rotation angle of φ in the *j*-th cone is the sum of errors generated in all x, y, and z axes such that

$$\hat{\phi}_j(\varphi) = \hat{\phi}_{x,j}(\varphi) + \hat{\phi}_{y,j}(\varphi) + \hat{\phi}_{z,j}(\varphi)\,. \tag{A.4}$$

Abbreviations

DESS	Double echo steady state
MSK	Musculoskeletal

MRI	Magnetic resonance imaging
FID	Free induction decay
UTE	Ultrashort echo time
UTE-DESS	UTE-based DESS
TR	Repetition time
FOV	Field of view
ECC	Eddy current correction
PR	Projection radial
LTI	Linear time invariant
NuFFT	Non-uniform fast Fourier transform
FA	Flip angle
rBW	Readout bandwidth
NEX	Number of excitations
PSF	Point spread function
GIRF	Gradient impulse response function
SPI	Single point imaging
ROIs	Regions of Interest

REFERENCES

1. Hardy PA, Recht MP, Piraino D, Thomasson D. Optimization of a Dual Echo in the Steady State (DESS) free-precession sequence for imaging cartilage. J. Magn. Reson. Imaging 1996;6:329–335 doi: 10.1002/jmri.1880060212. [PubMed: 9132098]
2. Welsch GH, Scheffler K, Mamisch TC, et al. Rapid estimation of cartilage T2 based on double echo at steady state (DESS) with 3 Tesla. Magn. Reson. Med. 2009;62:544–549 doi: 10.1002/mrm.22036. [PubMed: 19526515]
3. Moriya S, Miki Y, Yokobayashi T, Ishikawa M. Three-Dimensional Double-Echo Steady-State (3D-DESS) magnetic resonance imaging of the knee: Contrast optimization by adjusting flip angle. Acta radiol. 2009;50:507–511 doi: 10.1080/02841850902849444. [PubMed: 19353344]
4. Friedrich KM, Reiter G, Kaiser B, et al. High-resolution cartilage imaging of the knee at 3T: Basic evaluation of modern isotropic 3D MR-sequences. Eur. J. Radiol. 2011;78:398–405 doi: 10.1016/j.ejrad.2010.01.008. [PubMed: 20138723]
5. Siorpaes K, Wenger A, Bloecker K, Wirth W, Hudelmaier M, Eckstein F. Interobserver reproducibility of quantitative meniscus analysis using coronal multiplanar DESS and IWTSE MR imaging. Magn. Reson. Med. 2012;67:1419–1426 doi: 10.1002/mrm.23115. [PubMed: 22135245]
6. Moriya S, Miki Y, Matsuno Y, Okada M. Three-dimensional double-echo steady-state (3D-DESS) magnetic resonance imaging of the knee: establishment of flip angles for evaluation of cartilage at 1.5 T and 3.0 T. Acta radiol. 2012;53:790–794 doi: 10.1258/ar.2012.110532. [PubMed: 22850576]

7. Kohl S, Meier S, Ahmad SS, et al. Accuracy of cartilage-specific 3-Tesla 3D-DESS magnetic resonance imaging in the diagnosis of chondral lesions: comparison with knee arthroscopy. J. Orthop. Surg. Res. 2015;10:191 doi: 10.1186/s13018-015-0326-1. [PubMed: 26714464]
8. Chaudhari AS, Kogan F, Pedoia V, Majumdar S, Gold GE, Hargreaves BA. Rapid Knee MRI Acquisition and Analysis Techniques for Imaging Osteoarthritis. J. Magn. Reson. Imaging 2020;52:1321–1339 doi: 10.1002/jmri.26991. [PubMed: 31755191]
9. Muhle C, Ahn JM, Biederer J, et al. MR imaging of the neural foramina of the cervical spine: Comparison of 3D-DESS and 3D-FISP sequences. Acta radiol. 2002;43:96–100 doi: 10.1080/028418502127347510. [PubMed: 11972470]
10. Du R, Auguste KI, Chin CT, Engstrom JW, Weinstein PR. Magnetic resonance neurography for the evaluation of peripheral nerve, brachial plexus, and nerve root disorders. J. Neurosurg. 2010;112:362–371 doi: 10.3171/2009.7.JNS09414. [PubMed: 19663545]
11. Qin Y, Zhang J, Li P, Wang Y. 3D Double-Echo Steady-State with Water Excitation MR Imaging of the Intraparotid Facial Nerve at 1.5T: A Pilot Study. Am. J. Neuroradiol. 2011;32:1167–1172 doi: 10.3174/ajnr.A2480. [PubMed: 21566007]
12. Fujii H, Fujita A, Yang A, et al. Visualization of the peripheral branches of the Mandibular division of the trigeminal nerve on 3D double-echo steady-state with water excitation sequence. Am. J. Neuroradiol. 2015;36:1333–1337 doi: 10.3174/ajnr.A4288. [PubMed: 25836724]
13. Raval SB, Britton CA, Zhao T, et al. Ultra-high field upper extremity peripheral nerve and non-contrast enhanced vascular imaging Lin F-H, editor. PLoS One 2017;12:e0175629 doi: 10.1371/journal.pone.0175629. [PubMed: 28662061]
14. Burian E, Sollmann N, Ritschl LM, et al. High resolution MRI for quantitative assessment of inferior alveolar nerve impairment in course of mandible fractures: an imaging feasibility study. Sci. Rep. 2020;10:11566 doi: 10.1038/s41598-020-68501-5. [PubMed: 32665667]
15. Staroswiecki E, Granlund KL, Alley MT, Gold GE, Hargreaves BA. Simultaneous estimation of T 2 and apparent diffusion coefficient in human articular cartilage in vivo with a modified three-dimensional double echo steady state (DESS) sequence at 3 T. Magn. Reson. Med. 2012;67:1086–1096 doi: 10.1002/mrm.23090. [PubMed: 22179942]
16. Gras V, Farrher E, Grinberg F, Shah NJ. Diffusion-weighted DESS protocol optimization for simultaneous mapping of the mean diffusivity, proton density and relaxation times at 3 Tesla. Magn. Reson. Med. 2017;78:130–141 doi: 10.1002/mrm.26353. [PubMed: 27476684]
17. Sveinsson B, Chaudhari AS, Gold GE, Hargreaves BA. A simple analytic method for estimating T2 in the knee from DESS. Magn. Reson. Imaging 2017;38:63–70 doi: 10.1016/j.mri.2016.12.018. [PubMed: 28017730]
18. Sveinsson B, Gold GE, Hargreaves BA, Yoon D. SNR-weighted regularization of ADC estimates from double-echo in steady-state (DESS). Magn. Reson. Med. 2019;81:711–718 doi: 10.1002/mrm.27436. [PubMed: 30125389]
19. Chaudhari AS, Sveinsson B, Moran CJ, et al. Imaging and T2 relaxometry of short-T2 connective tissues in the knee using ultrashort echo-time double-echo steady-state (UTEDESS). Magn. Reson. Med. 2017;78:2136–2148 doi: 10.1002/mrm.26577. [PubMed: 28074498]
20. Jang H, Ma Y, Carl M, Jerban S, Chang EY, Du J. Ultrashort echo time Cones double echo steady state (UTE-Cones-DESS) for rapid morphological imaging of short T 2 tissues. Magn. Reson. Med. 2021;86:881–892 doi: 10.1002/mrm.28769. [PubMed: 33755258]
21. Vannesjo SJ, Haeberlin M, Kasper L, et al. Gradient system characterization by impulse response measurements with a dynamic field camera. Magn. Reson. Med. 2013;69:583–93 doi: 10.1002/mrm.24263. [PubMed: 22499483]
22. Jang H, Wiens CN, McMillan AB. Ramped hybrid encoding for improved ultrashort echo time imaging. Magn. Reson. Med. 2016;76:814–825 doi: 10.1002/mrm.25977. [PubMed: 26381890]
23. Jang H, McMillan AB. A rapid and robust gradient measurement technique using dynamic single-point imaging. Magn. Reson. Med. 2017;78:950–962 doi: 10.1002/mrm.26481. [PubMed: 27699867]
24. Atkinson IC, Lu A, Thulborn KR. Characterization and correction of system delays and eddy currents for MR imaging with ultrashort echo-time and time-varying gradients. Magn. Reson. Med. 2009;62:532–537 doi: 10.1002/mrm.22016. [PubMed: 19353662]

25. Harkins KD, Does MD, Grissom WA. Iterative Method for Predistortion of MRI Gradient Waveforms. IEEE Trans. Med. Imaging 2014;33:1641–1647 doi: 10.1109/TMI.2014.2320987. [PubMed: 24801945]
26. Brodsky EK, Klaers JL, Samsonov AA, Kijowski R, Block WF. Rapid measurement and correction of phase errors from B 0 eddy currents: Impact on image quality for non-cartesian imaging. Magn. Reson. Med. 2013;69:509–515 doi: 10.1002/mrm.24264. [PubMed: 22488532]
27. Duyn JH, Yang Y, Frank J a, van der Veen JW. Simple correction method for k-space trajectory deviations in MRI. J. Magn. Reson. 1998;132:150–153 doi: 10.1006/jmre.1998.1396. [PubMed: 9615415]
28. Ma Y, Jang H, Jerban S, et al. Making the invisible visible—ultrashort echo time magnetic resonance imaging: Technical developments and applications. Appl. Phys. Rev. 2022;9:041303 doi: 10.1063/5.0086459. [PubMed: 36467869]
29. Robison RK, Li Z, Wang D, Ooi MB, Pipe JG. Correction of B 0 eddy current effects in spiral MRI. Magn. Reson. Med. 2019;81:2501–2513 doi: 10.1002/mrm.27583. [PubMed: 30444004]
30. Spees WM, Buhl N, Sun P, Ackerman JJH, Neil JJ, Garbow JR. Quantification and compensation of eddy-current-induced magnetic-field gradients. J. Magn. Reson. 2011;212:116–123 doi: 10.1016/j.jmr.2011.06.016. [PubMed: 21764614]
31. Niederländer B, Blümler P. Simple eddy current compensation by additional gradient pulses. Concepts Magn. Reson. Part A 2018;47A:e21469 doi: 10.1002/cmr.a.21469.
32. Fessler JA. On NUFFT-based gridding for non-Cartesian MRI. J. Magn. Reson. 2007;188:191–195 doi: 10.1016/j.jmr.2007.06.012. [PubMed: 17689121]
33. Vannesjo SJ, Haeberlin M, Kasper L, et al. Image reconstruction using the gradient impulse response for trajectory prediction. Magn. Reson. Med. 2013;69:583–93 doi: 10.1002/mrm.24263. [PubMed: 22499483]
34. Freed DE, Scheven UM, Zielinski LJ, Sen PN, Hürlimann MD. Steady-state free precession experiments and exact treatment of diffusion in a uniform gradient. J. Chem. Phys. 2001;115:4249–4258 doi: 10.1063/1.1389859.
35. Jang H, Ma Y, Carl M, Jerban S, Chang EY, Du J. Ultrashort echo time Cones double echo steady state (UTE-Cones-DESS) for rapid morphological imaging of short T 2 tissues. Magn. Reson. Med. 2021;86:881–892 doi: 10.1002/mrm.28769. [PubMed: 33755258]
36. Bieri O, Ganter C, Scheffler K. Quantitative in vivo diffusion imaging of cartilage using double echo steady-state free precession. Magn. Reson. Med. 2012;68:720–729 doi: 10.1002/mrm.23275. [PubMed: 22161749]
37. Jang H, Liu F, Bradshaw T, McMillan AB. Rapid dual-echo ramped hybrid encoding MR-based attenuation correction (dRHE-MRAC) for PET/MR. Magn. Reson. Med. 2018;79:2912–2922 doi: 10.1002/mrm.26953. [PubMed: 28971513]
38. Bruce IP, Petty C, Song AW. Simultaneous and inherent correction of B0 and eddy-current induced distortions in high-resolution diffusion MRI using reversed polarity gradients and multiplexed sensitivity encoding (RPG-MUSE). Neuroimage 2018;183:985–993 doi: 10.1016/j.neuroimage.2018.09.055. [PubMed: 30243955]
39. Addy NO, Wu HH, Nishimura DG. Simple method for MR gradient system characterization and k-space trajectory estimation. Magn. Reson. Med. 2012;68:120–129 doi: 10.1002/mrm.23217. [PubMed: 22189904]
40. King KF, Ganin A, Zhou XJ, Bernstein M a. Concomitant gradient field effects in spiral scans. Magn. Reson. Med. 1999;41:103–112 doi: 10.1002/(SICI)1522-2594(199901)41:1<103::AID-MRM15>3.0.CO;2-M. [PubMed: 10025617]
41. Barmet C, Zanche N De, Pruessmann KP. Spatiotemporal magnetic field monitoring for MR. Magn. Reson. Med. 2008;60:187–197 doi: 10.1002/mrm.21603. [PubMed: 18581361]
42. Afsahi AM, Ma Y, Jang H, et al. Ultrashort Echo Time Magnetic Resonance Imaging Techniques: Met and Unmet Needs in Musculoskeletal Imaging. J. Magn. Reson. Imaging 2021:1–16 doi: 10.1002/jmri.28032.
43. Brandt KD, Radin EL, Dieppe PA, van de Putte L. Yet more evidence that osteoarthritis is not a cartilage disease. Ann. Rheum. Dis. 2006;65:1261–4 doi: 10.1136/ard.2006.058347. [PubMed: 16973787]

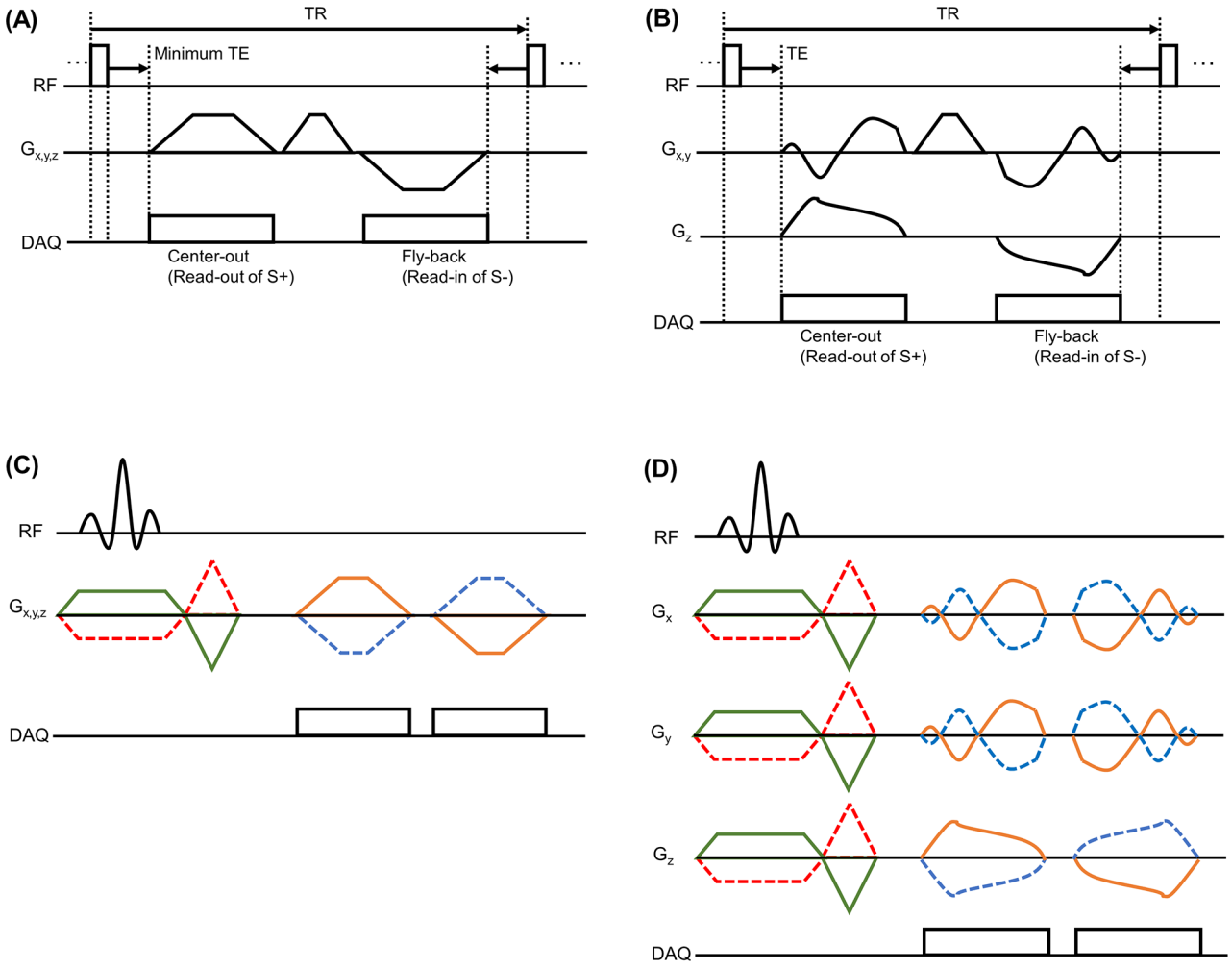

Figure 1.

A pulse sequence for UTE-DESS with 3D projection radial (PR) trajectory (A) and with 3D spiral cones trajectory (B), and pulse sequences used to correct for eddy currents in the so-called PR-mode (C) and the cones-mode (D). To simultaneously measure B_0 and linear eddy currents, the measurement is repeated four times with two different gradient polarities: G (orange lines in C and D), −G (blue lines in C and D), and two different slice locations, x_0 (green lines in C and D) and $-x_0$ (red lines in C and D). Note that the gradient is independently measured on each axis. (DAQ: data acquisition)

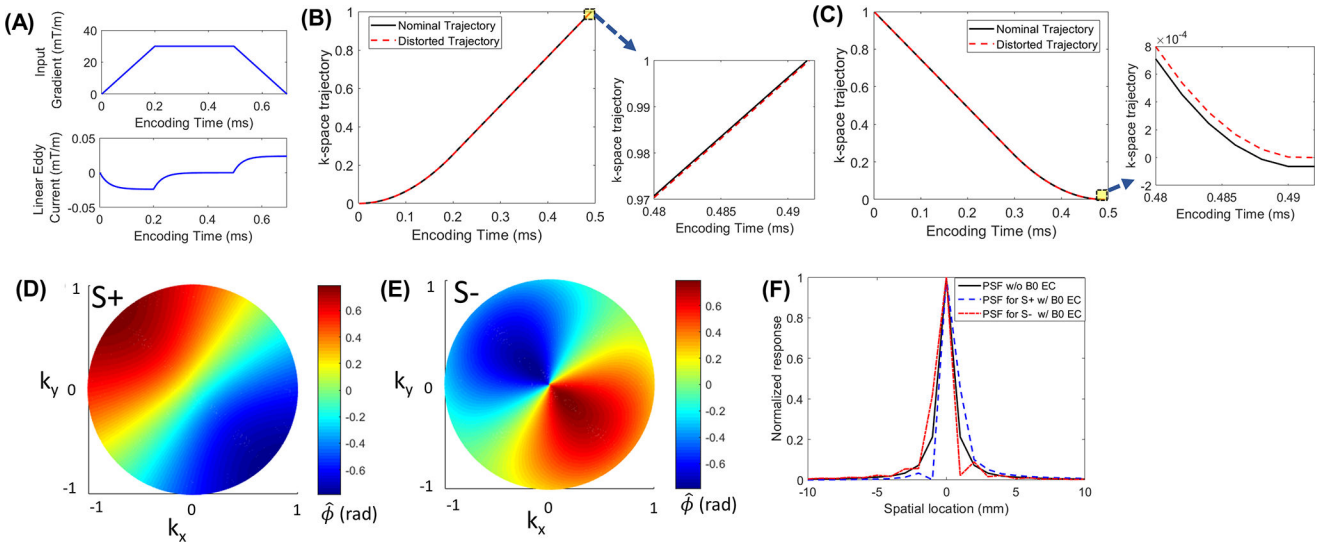

Figure 2.

Simulated eddy current. (A) The simulated linear eddy current, the nominal and distorted trajectories for (B) center-out S+ acquisition and (C) fly-back S− acquisition, simulated $\hat{\phi}$ caused by B_0 eddy current for (D) center-out S+ acquisition and (E) fly-back S− acquisition, and (F) central 1D profiles of the point spread functions (PSFs) simulated without or with the B_0 eddy current. The phase error in k-space appears in different shapes for S+ and S− in (D), which causes a shift of pixels in opposite directions, as shown in the simulated PSFs (F).

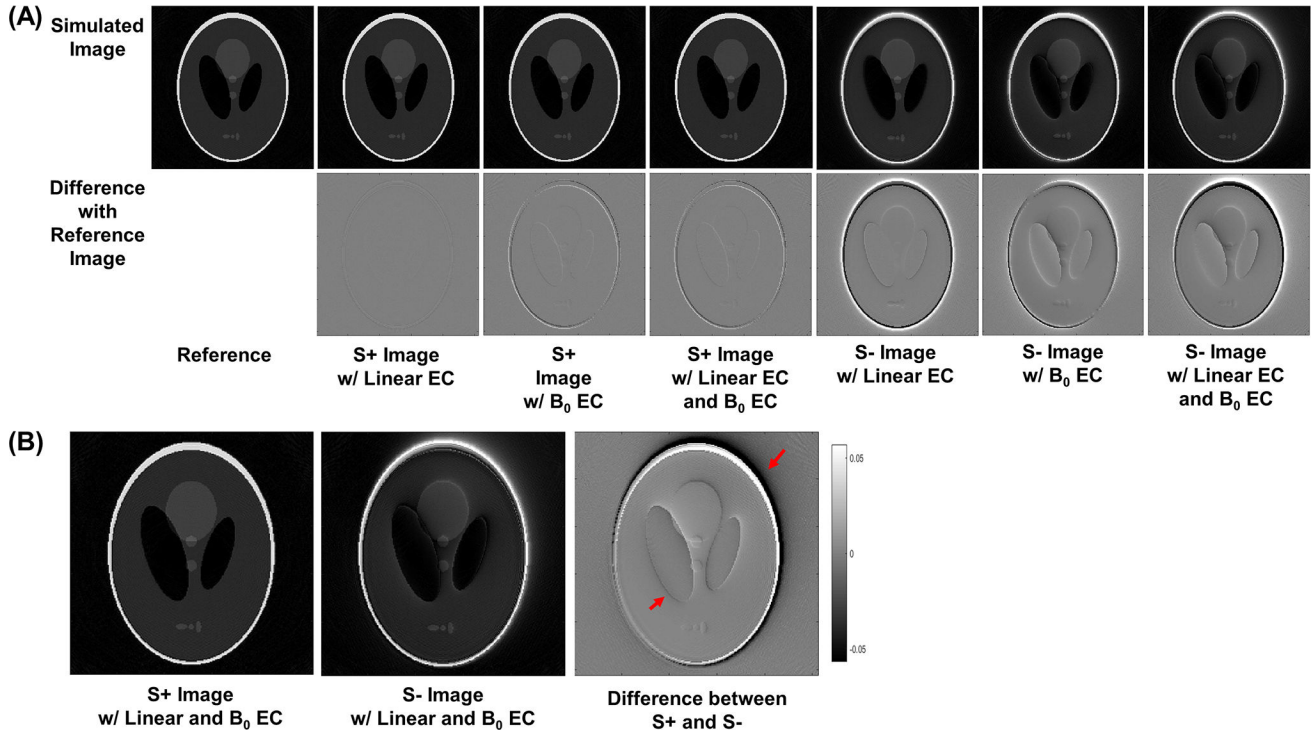

Figure 3.

Reconstructed images with simulated data. (A) Reconstructed images with simulated eddy current and the difference images with respect to a reference image reconstructed without eddy current, and (B) difference between the simulated S+ and S− images in the presence of linear and B_0 eddy currents. (EC: eddy current)

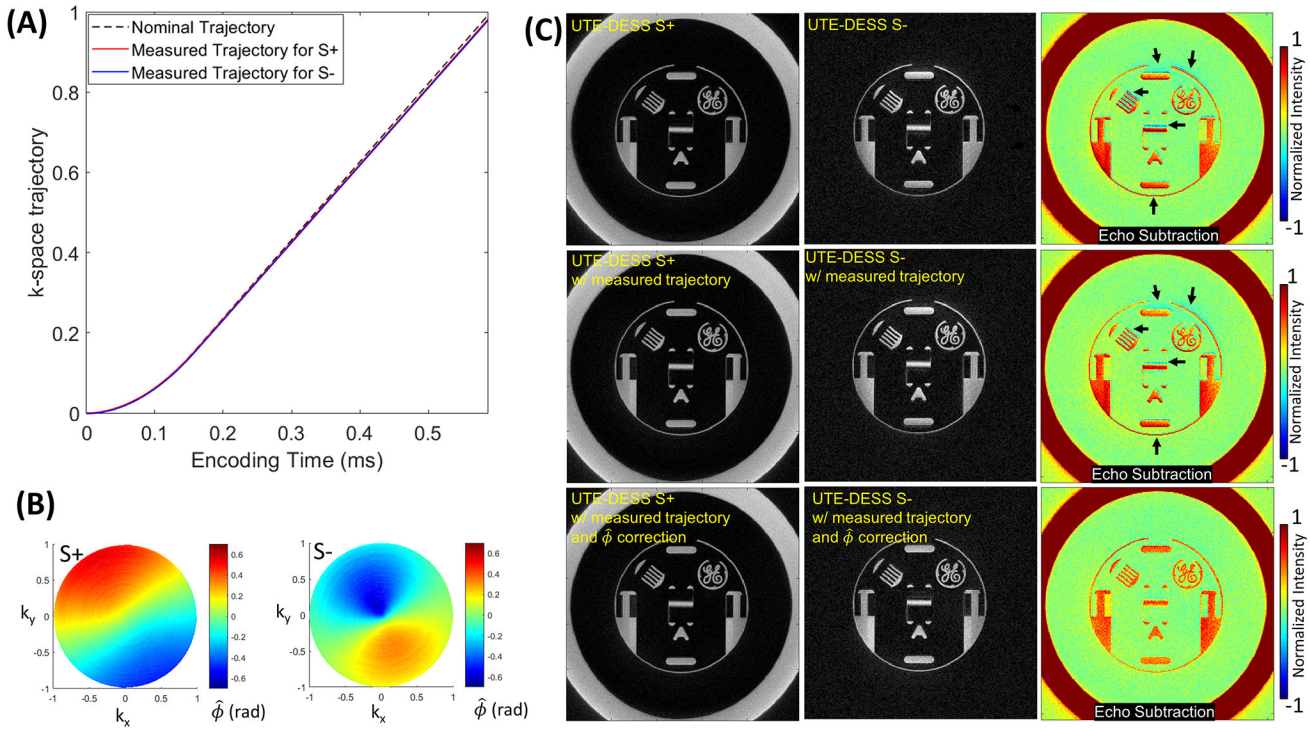

Figure 4.

Phantom experiment with PR-mode UTE-DESS. (A) An example of measured k-space trajectories, (B) $\widehat{\phi}$ for S+ or S− acquisition, and (C) reconstructed S+ and S− images without or with ECC, and the echo-subtracted images. The difference image without ECC shows strong boundary effect due to misalignment of pixels, an effect that is dramatically reduced by ECC removing the phase error across k-spaces (black arrows). The S− image is shown at 2x magnification in the lower window level.

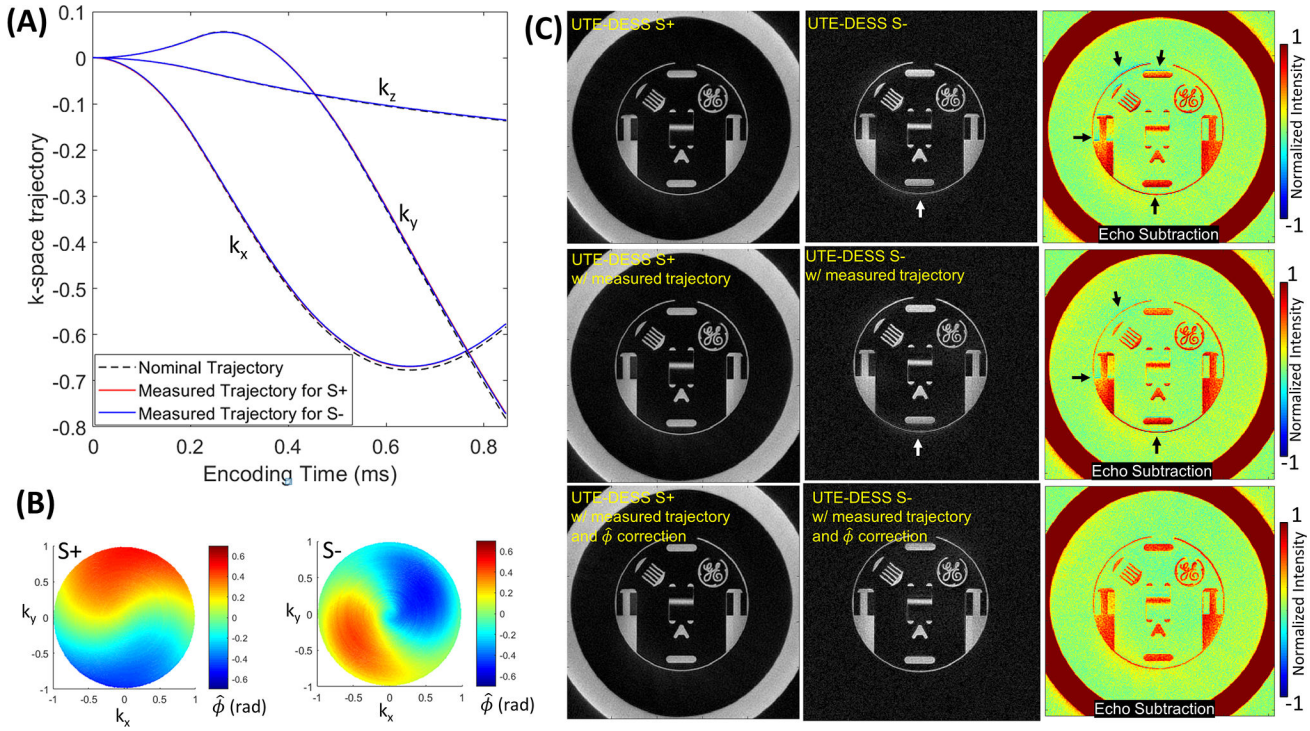

Figure 5.

Phantom experiment with cones-mode UTE-DESS. (A) An example of measured k-space trajectories, (B) $\hat{\phi}$ for S+ or S− acquisition, and (C) reconstructed S+ and S− images without or with ECC, and the echo-subtracted images. Spiral cones-mode shows weaker boundary effect than PR-mode. The remaining boundary effect (black arrows) and blurriness near boundary of the phantom are clearly removed by using both measured k-space trajectory and $\hat{\phi}$ (white arrows). The S− image is shown at 2x magnification in the lower window level.

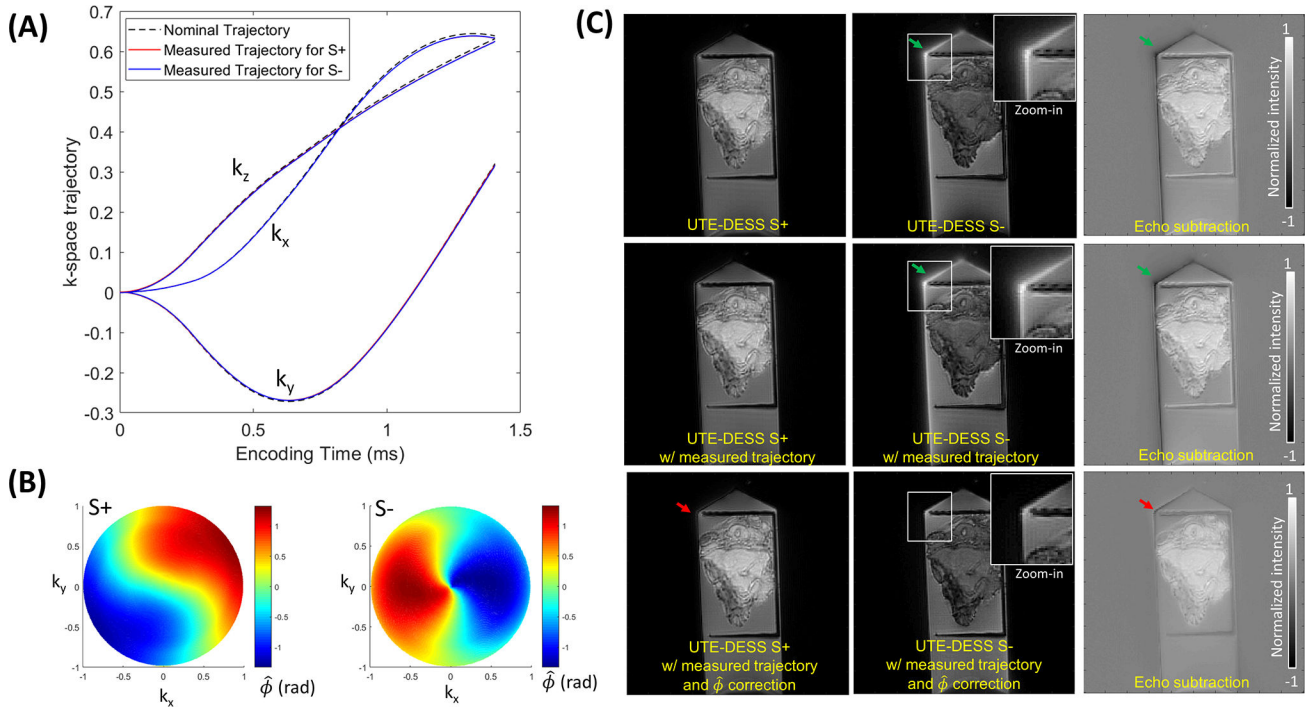

Figure 6.

Human synovium tissue with 3D cones-mode UTE-DESS (from a 60-year-old male patient with osteoarthritis). (A) An example of measured k-space trajectories, (B) $\hat{\phi}$ for S+ acquisition and S− acquisition, and (C) reconstructed S+ and S− images and the resultant echo subtraction image without or with ECC. With $\hat{\phi}$ correction, the artifact near the boundary of the syringe is suppressed (green arrow). The remaining error is visible presumably due to the imperfect ECC (red arrow).

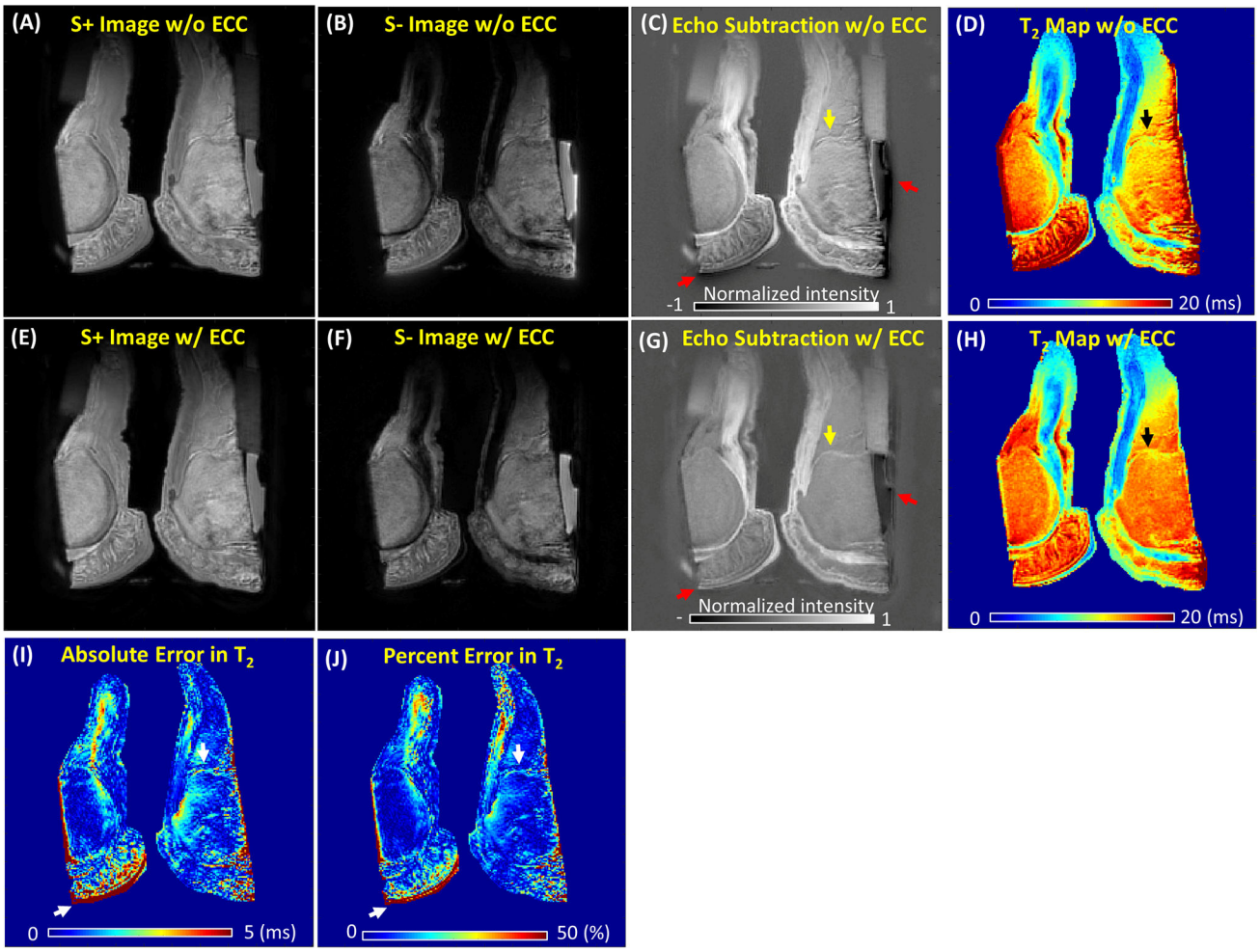

Figure 7.

Two cadaveric human ankles (left: 91-year-old female donor, right: 41-year-old female donor) imaged with the cones-mode UTE-DESS sequence: S+, S−, echo-subtracted images, the resultant T_2 map without ECC (A, B, C, D) and with ECC (E, F, G, H), and the absolute error (I) and percent error (J) calculated between T_2 maps without and with ECC. ECC significantly improves image quality in echo subtraction by removing misregistration of pixels (red arrows). Fine structures are more clearly detected with ECC (yellow and black arrows). In the T_2 maps, ECC corrects for boundary effects and low frequency bias across the samples. The error maps show strong error near tissue boundaries due to eddy current (white arrows).

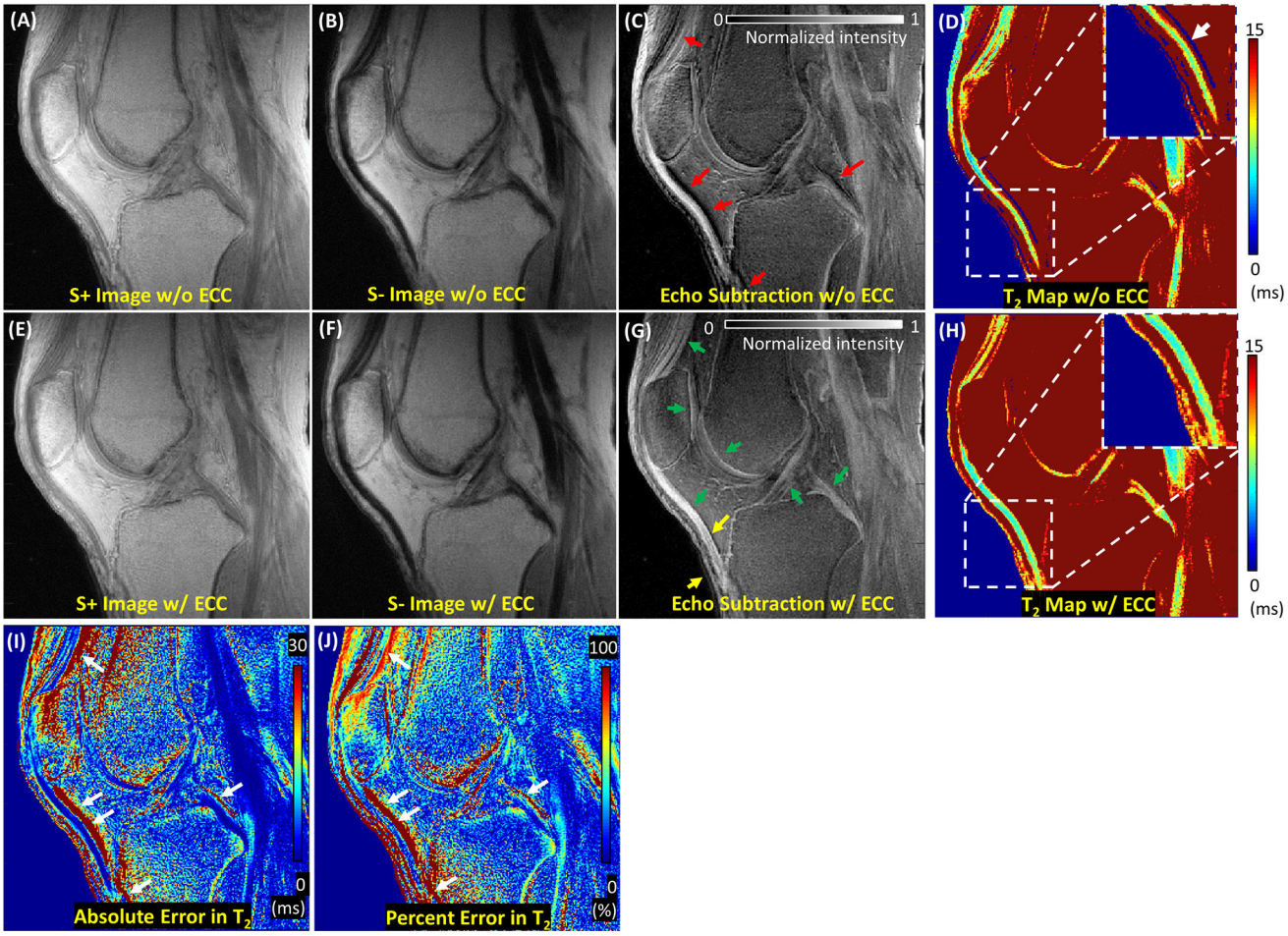

Figure 8.

In vivo knee imaging with cones-mode UTE-DESS (37-year-old male volunteer). S+, S−, echo-subtracted images, the resultant T_2 map without ECC (A, B, C, D) and with ECC (E, F, G, H), and the absolute error (I) and percent error (J) calculated between T_2 maps without and with ECC. ECC improved short T_2 contrast in the echo subtraction image with significantly suppressed boundary effects (red arrows), allowing more clear detection of tissues with short T_2 values (green arrows). Slight, uncorrected boundary effect is shown with ECC (yellow arrows). The T_2 map without ECC shows strong boundary artifacts where the estimated T_2 values are negative (blue pixels indicated by a white arrow in D), which are subsequently corrected with ECC. In I and J, strong errors are exhibited near the tissue boundaries due to the effects of eddy currents (white arrows). The T_2 map with ECC clearly shows the shape of the patellar tendon. In contrast, the T_2 map estimated without ECC shows a narrower and shorter profile of the patellar tendon due to either overestimation (the more distal patellar tendon) or underestimation (the posterior portion of the patellar tendon) at the boundary.